Discontinuous Galerkin time-domain computations of metallic nanostructures

Kai Stannigel[1,2,3], Michael König[1,2], Jens Niegemann[1,2], and Kurt Busch[1,2]

[1]*Institut für Theoretische Festkörperphysik, Universität Karlsruhe (TH), 76128 Karlsruhe, Germany*

[2]*DFG-Center for Functional Nanostructures (CFN), Universität Karlsruhe (TH), 76128 Karlsruhe, Germany*

[3]*Institute for Theoretical Physics, University of Innsbruck and Institute for Quantum Optics and Quantum Information, Austrian Academy of Sciences, Technikerstraße 25, 6020 Innsbruck, Austria*

kaist@tfp.uni-karlsruhe.de

Abstract: We apply the three-dimensional Discontinuous-Galerkin Time-Domain method to the investigation of the optical properties of bar- and V-shaped metallic nanostructures on dielectric substrates. A flexible finite element-like mesh together with an expansion into high-order basis functions allows for an accurate resolution of complex geometries and strong field gradients. In turn, this provides accurate results on the optical response of realistic structures. We study in detail the influence of particle size and shape on resonance frequencies as well as on scattering and absorption efficiencies. Beyond a critical size which determines the onset of the quasi-static limit we find significant deviations from the quasi-static theory. Furthermore, we investigate the influence of the excitation by comparing normal illumination and attenuated total internal reflection setups. Finally, we examine the possibility of coherently controlling the local field enhancement of V-structures via chirped pulses.

OCIS codes: (000.3860) Mathematical methods in physics; (000.4430) Numerical approximation and analysis; (240.6680) Optics at surfaces : Surface plasmons (260.3910) Physical optics : Metal optics; (290.5850) Scattering: Scattering, particles; (310.6628) Thin films : Subwavelength structures, nanostructures

References and links

1. T. Soller, M. Ringler, M. Wunderlich, T. A. Klar, J. Feldmann, H.-P. Josel, Y. Markert, A. Nichl, and K. Kürzinger, "Radiative and nonradiative rates of phosphors attached to gold nanoparticles," Nano Lett. **7**, 1941–1946 (2008).
2. J. Steidtner and B. Pettinger, "Tip-enhanced Raman spectroscopy and microscopy on single dye molecules with 15 nm resolution," Phys. Rev. Lett. **100**, 236101-1–4 (2008).
3. S. Kim, J. Jin., Y.-J. Kim, I.-Y. Park, Y. Kim, and S.-W. Kim, "High-harmonic generation by resonant plasmon field enhancement," Nature **453**, 757–760 (2008).
4. D. J. Bergman and M. I. Stockman, "Surface plasmon amplification by stimulated emission of radiation: Quantum generation of coherent surface plasmons in nanosystems," Phys. Rev. Lett. **90**, 027402-1–4 (2003).
5. N. I. Zheludev, S. I. Prosvirnin, N. Papasimakis, and V. A. Fedotov, "Lasing spaser," Nature Photon. **2**, 351–354 (2008).
6. M. Righini, A. S. Zelenina, C. Girard, and R. Quidant, "Parallel and selective trapping in a patterned plasmonic landscape," Nature Phys. **3**, 477–480 (2008).

#110638 - $15.00 USD Received 27 Apr 2009; revised 12 Jun 2009; accepted 26 Jun 2009; published 7 Aug 2009

7. M. Righini, V. Giovani, C. Girard, D. Petrov, and R. Quidant, "Surface plasmon optical tweezers: Tunable optical manipulation in the femtonewton range," Phys. Rev. Lett. **100**, 186804-1–4 (2008).
8. A. N. Grigorenko, N. W. Roberts, M. R. Dickinson, and Y. Zhang, "Nanometric optical tweezers based on nanostructured substrates," Nature Photon. **2**, 365–370 (2008).
9. M. Aeschlimann, M. Bauer, D. Bayer, T. Brixner, F. J. Garcia de Abajo, W. Pfeiffer, M. Rohmer, C. Spindler, and F. Steeb, "Adaptive subwavelength control of nano-optical fields," Nature **446**, 301–304 (2007).
10. P. B. Johnson and R. W. Christy, "Optical constants of the noble metals," Phys. Rev. B **6**, 4370–4379 (1972).
11. C. M. Aikens, S. Li, and G. C. Schatz, "From discrete electronic states to plasmons: TDDFT optical absorption properties of Ag_n(n=10,20,35,56,84,120) tetrahedral clusters," J. Phys. Chem. C **112**, 11272–11279 (2008).
12. M. I. Stockman, S. V. Faleev, and D. J. Bergman, "Coherent control of femtosecond energy localization in nanosystems," Phys. Rev. Lett. **88**, 067402-1–4 (2002).
13. M. I. Stockman, D. J. Bergmann, and T. Kobayashi, "Coherent control of nanoscale localization of ultrafast optical excitation in nanosystems," Phys. Rev. B **69**, 054202–054211 (2004).
14. X. Li and M. I. Stockman, "Highly efficient spatiotemporal control in nanoplasmonics on a nanometer-femtosecond scale by time reversal," Phys. Rev. B **77**, 195109 (2008).
15. V. Myroshnychenko, J. Rodriguez-Fernandez, I. Pastoriza-Santos, A. M. Funston, C. Novo, P. Mulvaney, L. M. Liz-Martin, and F. J. Garcia de Abajo, "Modelling the optical response of gold nanoparticles," Chem. Soc. Rev. **37**, 1792–1805 (2008).
16. J. Jin, *Computational Electrodynamics: The Finite Element Method in Electromagnetics* (2nd edition, John Wiley & Sons, New York, 2002).
17. C. Hafner, *Post-modern Electromagnetics* (John Wiley & Sons, New York, 1999).
18. N. Calander and M. Willander, "Theory of surface-plasmon resonance optical-field enhancement at prolate spheroids," J. Appl. Phys. **92**, 4878–4884, (2002).
19. R. Kappeler, D. Erni, C. Xudong, and L. Novotny, "Field computations of optical antennas," J. Comput. Theor. Nanosci. **4**, 686–691 (2007).
20. X. Cui, W. Zhang, B.-S. Yeo, R. Zenobi, Ch. Hafner, and D. Erni, "Tuning the resonance frequency of Ag-coated dielectric tips," Opt. Express **15**, 8309–8316 (2007).
21. H. Fischer and O. J. F. Martin, "Engineering the optical response of plasmonic nanoantennas," Opt. Express **16**, 9144–9154 (2008).
22. M. I. Stockman, "Ultrafast nanoplasmonics under coherent control," New J. Phys. **10**, 025031 (2008).
23. A. Taflove and S. C. Hagness, *Computational electrodynamics* (3rd edition, Artech House, Boston, 2005).
24. J. Niegemann, M. König, K. Stannigel, and K. Busch, "Higher-order time-domain methods for the analysis of nano-photonic systems," Photon. Nanostruct. Fundam. Appl. **7**, 2–11 (2008).
25. J. S. Hesthaven and T. Warburton, "Nodal high-order methods on unstructured grids - I. Time-domain solution of Maxwell's equations," J. Comput. Phys. **181**, 186–221 (2002).
26. T. Lu, P. Zhang, and W. Cai, "Discontinuous Galerkin methods for dispersive and lossy Maxwell's equations and PML boundary conditions," J. Comput. Phys. **200**, 549–580 (2004).
27. M. H. Carpenter and C. A. Kennedy, "Fourth-Order 2N-Storage Runge-Kutta Schemes," Technical Report NASA-TM-109112, NASA Langley Research Center, VA (1994).
28. K. Busch, J. Niegemann, M. Pototschnig, and L. Tkeshelashvili, "A Krylov-subspace based solver for the linear and nonlinear Maxwell equations," phys. stat. sol. (b) **244**, 3479–2496 (2007).
29. H. C. van de Hulst, *Light scattering by small particles* (Dover Publ., New York, 1981).
30. M. Liu, P. Guyot-Sionnest, T.-W. Lee, and S. K. Gray, "Optical properties of rodlike and bipyramidal gold nanoparticles from three-dimensional computations," Phys. Rev. B **76**, 235428 (2007).
31. E. Hao and G. C. Schatz, "Electromagnetic fields around silver nanoparticles and dimers," J. Chem. Phys. **120**, 357–366 (2004).
32. H. Kuwata, H. Tamaru, K. Esumi, and K. Miyano, "Resonant light scattering from metal nanoparticles: Practical analysis beyond Rayleigh approximation," Appl. Phys. Lett. **83**, 4625–4627 (2003).
33. C. F. Bohren and D. R. Huffman, *Absorption and scattering of light by small particles* (John Wiley & Sons, New York, 1983).
34. C. Sonnichsen, S. Geier, N. E. Hecker, G. von Plessen, J. Feldmann, H. Ditlbacher, B. Lamprecht, J. R. Krenn, F. R. Aussenegg, V. Z-H. Chan, J. P. Spatz, and M. Moller, "Spectroscopy of single metallic nanoparticles using total internal reflection microscopy," Appl. Phys. Lett. **77**, 2949–2951 (2000).
35. A. Arbouet, D. Christofilos, N. Del Fatti, F. Vallée, J.R. Huntzinger, L. Arnaud, P. Billaud, and M. Broyer, "Direct Measurement of the Single-Metal-Cluster Optical Absorption," Phys. Rev. Lett. **93**, 127401-1–4 (2004).
36. M. Husnik, M. W. Klein, N. Feth, M. König, J. Niegemann, K. Busch, S. Linden, and M. Wegener, "Absolute extinction cross-section of individual magnetic split-ring resonators," Nature Photon. **2**, 614–617 (2008).

#110638 - $15.00 USD Received 27 Apr 2009; revised 12 Jun 2009; accepted 26 Jun 2009; published 7 Aug 2009

1. Introduction

The relevant property of metals with respect to their optical response is the large density of free electrons. Under appropriate excitation conditions, these electrons undergo coherent collective oscillations relative to a rather immobile background of positively charged ions. The confined geometry provided by metallic nanostructures allows for the resonant enhancement of a discrete set of so-called particle plasmon resonances. These lead to large electric fields and strong field gradients which may be exploited for numerous applications. In an optical context, the excitation may be realized, for instance, via an external light source. The resulting strongly localized fields lead to enhanced fluorescence from molecules [1], facilitate tip-enhanced Raman-scattering spectroscopy techniques [2] and on-chip generation of high harmonics [3]. They even allow for coherently amplified radiation based on novel principles such as the spaser [4] and the lasing spaser [5]. Similarly, the strong field gradients associated with plasmonic nanostructures start to find applications in novel types of optical tweezers [6–8]. Furthermore, it has recently been demonstrated experimentally that the utility of metallic nanostructures may be considerably enhanced through controlled excitation with shaped beams [9]. In fact, the current state-of-the-art in realizing beams with prescribed temporal profile in phase, amplitude, and polarization will allow a far-reaching control over the spatio-temporal localization of radiation for the applications discussed above.

This clearly demonstrates an elevated need for quantitative theoretical understanding on various levels of sophistication. In fact, a large forest of theoretical and computational methods has been brought to bear on this problem. These include the choice of material models and approaches to improve the accuracy of representing the nanostructures' geometries and associated electromagnetic fields. For instance, on the linear optical level, metals may be described as dispersive and, hence, absorptive dielectric materials with spatially local responses. In many relevant cases this amounts to employing the celebrated Drude or Drude-Lorentz models [10]. On the other hand, if non-radiative processes such as the charge-transfer between molecules and metallic nanostructures in surface- or tip-enhanced Raman scattering become relevant, fully quantum mechanical calculations, e.g., via Time-Dependent Density-Functional Theory (TDDFT) can be employed [11]. Clearly, more complex material models quickly require rather significant computational resources so that typically only very small metal clusters can be treated via TDDFT.

Even within a linear material model, there exists a large variety of approaches that range from the quasi-static approximation for sufficiently small particles [12–14] all the way to full Maxwell solvers (for a recent review, see [15]). Broadly speaking, the latter may be divided further into frequency-domain and time-domain methods. Most frequency-domain methods such as Boundary Element Methods [16], Multiple Multipole Methods [17], and the Finite Element Methods [16] lend themselves to highly accurate representations of complex geometries. Many different systems have been studied—mostly driven by what can be realized experimentally and often guided by antenna design principles [7, 15, 18–21]. However, certain applications, for instance those that employ shaped beams [9] and/or coherent control principles [14, 22], are more naturally treated within a time-domain framework. Surprisingly and in contrast to the numerous frequency-domain methods, the choice of time-domain methods for the treatment of nano-photonic problems is rather limited, the Finite-Difference Time-Domain method undoubtedly being the most popular one [23].

In this paper, we present our analysis of the optical properties of experimentally feasible bar- and V-shaped metallic nanostructures using our implementation [24] of the recently developed three-dimensional Discontinuous-Galerkin Time-Domain (DGTD) method [25]. In essence, the DGTD approach combines a finite-element-like representation of complex geometries with an explicit time-stepping capability: An adaptive high-order spatial discretization allows for the

#110638 - $15.00 USD Received 27 Apr 2009; revised 12 Jun 2009; accepted 26 Jun 2009; published 7 Aug 2009

use of a corresponding high-order time-integration scheme so that the resulting solver is very well suited for the quantitative analysis of complex nano-photonic systems.

The remainder of this paper is structured as follows: In section 2, we present a brief introduction to the DGTD method, while a validation of our implementation is provided in section 3, where we compare numerical results for metallic spheres with analytic Mie theory. In sections 4 and 5, we analyze, respectively, nanoscopic silver bars and V-shaped structures with regard to their size-dependent properties such as resonance frequencies and attainable field enhancements under various excitation conditions.

2. The discontinuous Galerkin time-domain method

In this section, we provide a brief outline of the basic ideas underlying the DGTD method. For more details and the relevant formulas, we refer the reader to Refs. [24–26].

The key feature of the DGTD method is that it allows to use an explicit time-stepping scheme in combination with a finite-element discretization. The starting point of each calculation is thus the tessellation of the computational domain by finite elements, which in our case are straight-sided tetrahedra. Then, on each element the components of the electromagnetic field are expanded into polynomials of adjustable order p. In contrast to the classical finite element method [16], this expansion is purely local and the fields are allowed to be discontinuous across element boundaries. In order to facilitate the coupling between neighboring elements, one introduces an additional penalty term, which weakly enforces the physical boundary conditions.

As a consequence of this procedure, we obtain a large system of coupled ordinary differential equations (ODEs) for the expansion coefficients of the electromagnetic field. Since this system consists of small independent blocks related to the individual elements, it can be readily integrated using an explicit time-stepping scheme. For the calculations presented in this work, we employed a standard 4th-order low-storage Runge-Kutta algorithm as described in Ref. [27]. However, since within DGTD the time-stepping is essentially disentangled from the spatial discretization (as opposed to the situation in FDTD), more sophisticated methods such as Krylov-subspace based operator exponential techniques [28] could provide an even more efficient solver.

For practical computations, the basic algorithm sketched above needs to be complemented by various extensions. For instance, Lu et al. [26] have shown how to implement dispersive materials and perfectly matched layer (PML) absorbing boundary conditions via auxiliary differential equations. The performance of the PMLs has been optimized in Ref. [24]. Finally, the well-known total-field/scattered-field approach [23] for the injection of pulses into a scattering configuration can directly be used in DGTD.

3. Scattering by a metallic sphere

In order to validate our implementation and as a benchmark problem we calculate the total scattering and absorption cross sections of a metallic sphere. The dispersion of the metal is modeled as a standard Drude response given by

$$\varepsilon(\omega) = 1 - \frac{\omega_d^2}{\omega(\omega - i\gamma_d)},$$

where the plasma frequency $\omega_d = 1.39 \cdot 10^{16} s^{-1}$ and the collision rate $\gamma_d = 3.23 \cdot 10^{13} s^{-1}$ correspond to the values given by Johnson and Christy [10] for silver. However, it should be noted that these values underestimate the losses in the ultraviolet regime. We take the sphere to have a radius of 50nm and to be embedded in vacuum.

#110638 - $15.00 USD Received 27 Apr 2009; revised 12 Jun 2009; accepted 26 Jun 2009; published 7 Aug 2009

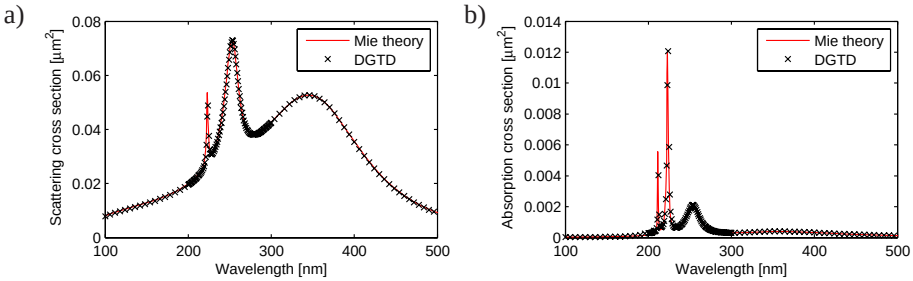

Fig. 1. (a) Scattering and (b) absorption cross sections of a silver sphere with radius 50nm embedded in vacuum. The computations involve 2750 tetrahedra for the sphere itsself and have been performed with interpolation polynomials of order $p = 3$. The results agree well with analytic Mie theory. See the text for further details.

A sketch of the computational setup is shown in Fig. 2(a): In order to simulate an open system, the computational domain is terminated by uniaxial perfectly matched layers (PMLs) [24]. Furthermore, it is divided into a total-field and a scattered-field (TF/SF) region, where at the interface between these regions a broad band pulse is injected into the TF region [23]. At the same interface we record the Fourier components of the Poynting vector both inside and outside the TF region. An integration and subsequent normalization to the incident spectrum then yields scattering and absorption cross sections, respectively.

When carrying out such computations one has considerable freedom in choosing various parameters. We have performed our computations with varying orders of the spatial discretization ($p = 3, 4$), different numbers of tetrahedra for the sphere (in five steps from 160 to 2750) and different sizes of the PML region (either one or two cells). Although we find that the interpolation order and the size of the PML do have a slight influence on the accuracy of the result, the error is strongly dominated by the tetrahedrization of the sphere. This result has been anticipated, since we are using straight-sided elements which essentially lead to a polygonal approximation of the sphere's shape. In Fig. 1, we display the results for the scattering and absorption cross sections for a computation when the sphere is meshed with 2750 tetrahedra and where a third-order spatial discretization is used. A comparison with analytic Mie theory [29] shows that the relative pointwise error of the spectrum is below 2 % except in the region of the highest resonance, where the error is significant (up to 10%) even for the finest discretization. This indicates that for the reproduction of the exact position and strength of high-Q resonances, one should resort to curved elements or much finer discretizations. For lower-Q resonances as well as for the general structure of the spectrum the presented calculations yield well-converged results.

4. Optical properties of silver nano-bars

As a more practical example we study silver nano-bars that are positioned on a glass substrate. Such structures may serve as optical antennas for concentrating light on the sub-wavelength scale and, thus, are of considerable interest for applications that include nonlinear spectroscopy or optical tweezing.

In Fig. 2(b) we display the bar's geometric model which features a realistic rounding with radius $r_{\text{end}} = w/2$ at the endings of the bar. In this context, we would like to point out that the finite-element discretization allows us to model the rounding without staircasing as would be the case within standard FDTD. While this might be of limited relevance in the case of a

#110638 - $15.00 USD Received 27 Apr 2009; revised 12 Jun 2009; accepted 26 Jun 2009; published 7 Aug 2009

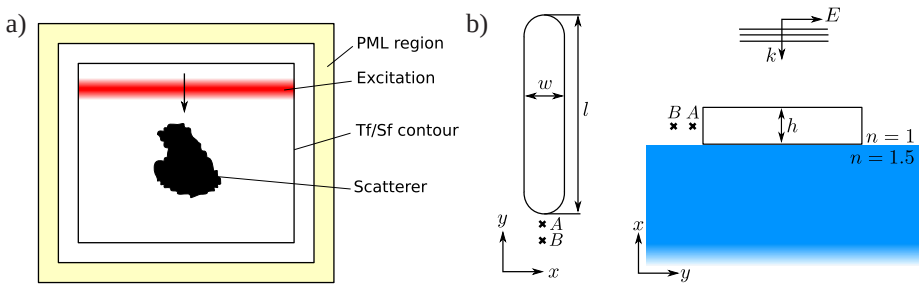

Fig. 2. (a) Sketch of the general computational setup for computing the optical properties of metallic nanostructures. (b) Dimensions of a nano-bar that is positioned on a glass substrate. The two points *A* and *B* mark the recording sites for the electric field enhancements (not to scale).

bar-shaped object, it certainly is of high relevance for a V-shaped object as discussed in section 5.

For this setup, we compute the field enhancement factors upon plane wave excitation and also investigate the question of the onset of the quasi-static limit, i.e., we determine the maximum size for which the properties of the bar are well described by a purely electrostatic calculation. In fact, local field enhancements near rod-shaped or spheroidal metallic nanoparticles have been considered before by other authors (see e.g. Refs. [18,19,30,31]). However, our computations take into account that in most experimental realizations nano-particles are deposited onto a dielectric substrate. Furthermore, we determine the dependence of the achievable enhancement on particle size which serves as a reference for the V-structure that we consider in section 5.

4.1. Local field enhancement

For the computation of the field enhancement just before the tips of a nano-bar we proceed as follows: We determine the (lowest) resonance frequency f_{res} of the structure by recording the scattering and absorption cross sections as described in section 3. Then, in a second computation, we irradiate the structure by a monochromatic plane wave with the very resonance frequency, where the amplitude is slowly ramped up from zero to its final value. This time, we record the values of the fields in front of the tip. The simulation is stopped when the enhancement has saturated. For the systems described below, this takes approximately 30 optical cycles (cf. Fig. 3(a)). We have carried out these computations for bars of fixed widths and heights, $w = h =$20nm, and whose lengths range between $l =$ 100–200nm. Figure 3(b) shows the extracted enhancements 10nm above the substrate at sites *A* and *B* that are located 1nm and 5nm away from the tip, respectively (c.f. Fig. 2(b)). To check whether our results are converged, we have performed all calculations with interpolation orders $p = 2$ and $p = 3$. Finally, for completeness we provide in Table 1 the wavelengths λ_{res} corresponding to the lowest resonance frequencies as well as the respective quality factors *Q* for different bars.

4.2. Quasi-static limit

Inspired by the popularity of quasi-static calculations of the optical properties of metallic nanostructures and the numerous exciting predictions that have been made for such systems [12–14, 32], we seek to find the maximum size of a nano-bar for which such a description is still adequate. We will present the discussion in terms of the experimentally accessible scattering and absorption efficiencies, which we obtain by normalizing the corresponding cross

#110638 - $15.00 USD Received 27 Apr 2009; revised 12 Jun 2009; accepted 26 Jun 2009; published 7 Aug 2009

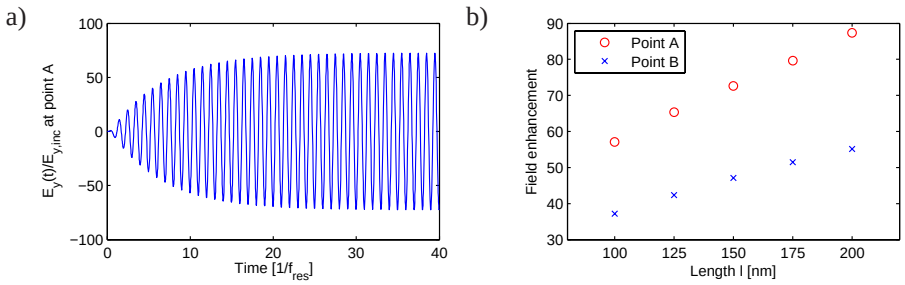

Fig. 3. Local field enhancements for silver nano-bars on glass substrates: Panel (a) displays the saturation of the recorded time signal for the y-component of the electric field at point A (bar length $l = 150$nm). Panel (b) shows the extracted values of the field enhancement at points A and B for bars of different lengths l (see Fig. 2 for further details of the system).

Table 1. Lowest frequency resonance wavelengths λ_{res} and corresponding quality factors Q for nano-bars with different lengths l and fixed width and height, $w = h = 20$nm.

l [nm]	100	125	150	175	200
λ_{res} [nm]	750	880	1008	1136	1260
Q	22.2	20.6	19.4	18.7	18.1

sections to the geometric cross section of the object normal to the incident beam.

Before analyzing the nano-bars, it is instructive to first consider the case of a metallic sphere with permittivity $\varepsilon(\omega)$ and unit permeability for which the efficiencies in the quasi-static limit can be determined analytically as [33]

$$Q_{\text{sca}} = \frac{8}{3}x^4\left|\frac{\varepsilon(\omega)-1}{\varepsilon(\omega)+2}\right|^2, \qquad Q_{\text{abs}} = 2x\,\text{Im}\left\{\frac{\varepsilon(\omega)-1}{\varepsilon(\omega)+2}\right\} \qquad \text{for } x = ka \ll 1.$$

Here, k is the wave vector of the incident light and a the radius, i.e., the characteristic length, of the particle. The above expressions inform us that the spectral profile of the efficiencies—and in particular the position of the resonance—is independent of the particle *size*, but rather depends on the particle *shape*. The size merely influences the magnitudes of the efficiencies. In fact, this statement is true for scatterers of arbitrary shape. Thus, the quasi-static limit is reached if the resonance frequency of the particle is size independent and the efficiencies scale as $Q_{\text{sca}} \propto a^4$ and $Q_{\text{abs}} \propto a$ with the particle's characteristic length a. Note that we are not considering the cross sections which would scale with an additional factor of a^2 each.

In order to address the question whether the nano-bars are in the quasi-static limit, we perform a scaling analysis and check for the above criteria: We start with a specific structure and compute its spectral response near the resonance frequency. Then, we scale all dimensions by a common factor $s < 1$, and repeat the computations. The behavior of the efficiencies as a function of the scaling factor s can be used to detect the onset of the quasi-static limit. For simplicity, we reduce the shape of the nano-bar to a rectangular box with sharp corners. This reduces the computational effort since small tetrahedra in the rounded endings of the bars limit the simulation time-step. At the same time, while details of the individual structures slightly differ, the scaling behavior for rounded bars and bars with sharp corners can be assumed to be the same.

#110638 - $15.00 USD Received 27 Apr 2009; revised 12 Jun 2009; accepted 26 Jun 2009; published 7 Aug 2009

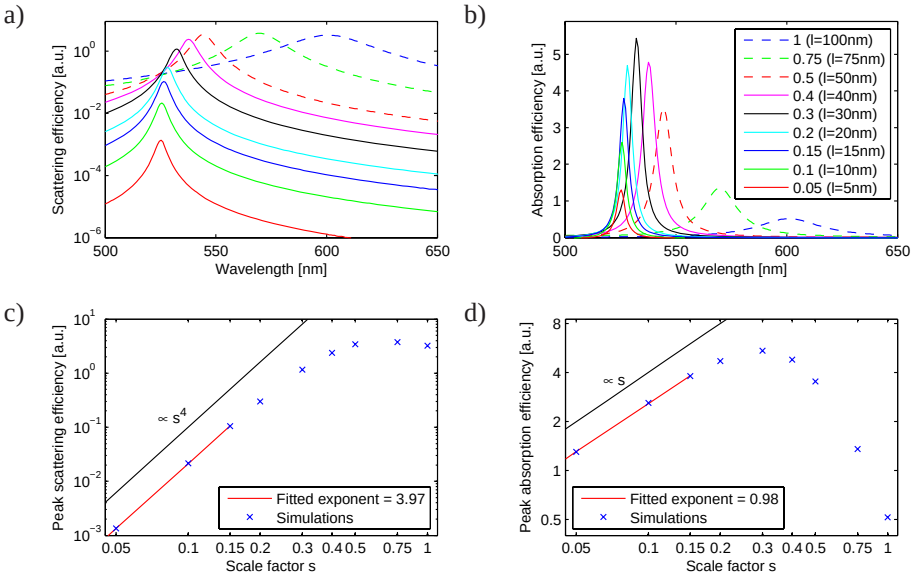

Fig. 4. Scaling analysis for a nano-bar with reference geometry parameters $l = 100$nm and $w = h = 25$nm (see Fig. 2). The graphs show the behavior of (a) the scattering and (b) the absorption efficiencies upon scaling of this reference geometry by a common factor s, which is given for both panels in the legend of (b). Panels (c) and (d) show the peak values of the respective efficiencies as a function of the scaling factor on a double-logarithmic scale. A linear fit to the three data points that correspond to the smallest structures is used to determine the exponent of the power-law dependence. The units for the efficiencies are the same in all graphs.

On the technical side, we proceed as in the previous section to determine the cross sections. When scaling the system down, we rescale only the bar itsself, while we keep the computational domain unchanged in size. This ensures that the PMLs do not become drastically smaller than the resonant wavelength and, therefore, our procedure avoids spurious reflections. Furthermore, we design the mesh in such a way that bars with different scaling factors s consist of approximately the same number of tetrahedra so that we do not loose any accuracy. As a result, the simulation timestep (which is proportional to the size of the smallest tetrahedron) is proportional to the scaling factor and, thus, the required CPU-time is inversely proportional to the scaling factor. In order to save computational resources, the two symmetry planes of the problem were exploited to reduce the number of elements by a factor of 1/4.

In Fig. 4, we display the results for the scaling of a bar with a reference geometry of $100 \times 25 \times 25\text{nm}^3$ down to 5% of its original size. For simplicity, we omit the dielectric substrate in these calculations. From the overview plots Fig. 4(a) and Fig. 4(b), we observe the well-known fact that absorption in small particles dominates over scattering. With regard to the first criterion formulated above, we notice that the position of the resonance saturates for scaling factors $s \leq s_{\text{crit}} \approx 0.15$. Regarding the second criterion, we deduce the power law dependence of the cross sections from panels (c) and (d). Consistent with the first criterion, we find the same critical scaling factor $s_{\text{crit}} \approx 0.15$. Therefore, we conclude that for the setup consisting of silver nano-bars in vacuum, the quasi-static limit in the sense defined above sets in for structures with spatial extensions as small as $l \lesssim 15$nm.

#110638 - $15.00 USD Received 27 Apr 2009; revised 12 Jun 2009; accepted 26 Jun 2009; published 7 Aug 2009

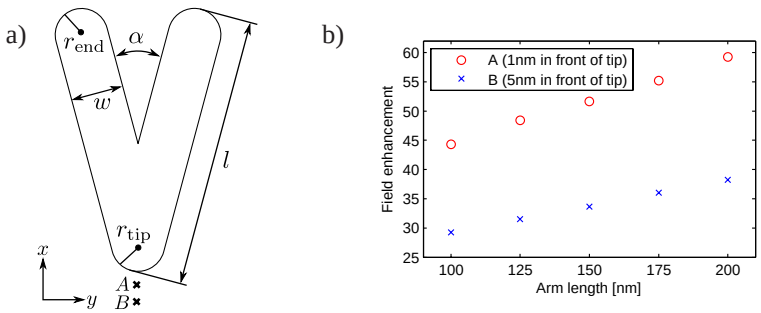

Fig. 5. (a) Sketch of the setup used for the V-structure computations. The radii of the tips and the arm edges are taken to be half of the arm width w unless otherwise noted. For the calculation of the field enhancements the structure is placed on a glass substrate and the fields are recorded at points A and B. Again, A (B) is located half the height of the metal film above the substrate and 1nm (5nm) away from the tip. (b) Summary of the extracted enhancements at the two sites A and B for V-structures of different lengths l, fixed width and height, $w = h = 20$nm, and fixed apex angle $\alpha = 30^\circ$.

5. Optical properties of silver V-shaped nanostructures

As a second example, we consider V-shaped structures, which have been extensively analyzed by Stockman et. al. [12, 13] using a quasi-static approach. In fact, these authors have found that such systems lend themselves to realizing strong local-field enhancements at their tips. In view of our scaling analysis for the nano-bars and the resulting experimental challenges in fabricating high-quality structures of corresponding size, we perform our analysis for the full Maxwell equations. This allows us to understand how the results of the quasi-static analysis manifest themselves in experimentally more accessible systems.

In Fig. 5(a) we depict the setup that we use for the V-structure computations throughout this section. Except for the nanostructure the computational setup including the material parameters is the same as in the previous section. We regard this setup as quite realistic since it includes smooth edges which inevitably arise when such structures are fabricated via focussed ion beam facilities or using electron beam lithography. Again, we want to point out that the adaptive finite-element discretization allows us to model the structure without introducing unphysically sharp edges. In contrast to the bar-geometry, the rounded edges at the tips of the Vs do, however, make a significant difference when compared to the corresponding cases with infinitely sharp tips.

5.1. Local field enhancement

In analogy with the analysis of the nano-bar structures, we first determine the local field enhancements at positions A and B that are, respectively, located 1nm and 5nm in front of the tip and $h/2$ above the glass substrate. We list the resonance wavelengths and corresponding Q-factors for the lowest frequency resonance of V-structures with different lengths, fixed $w = h = 20$nm, and fixed apex angle $\alpha = 30^\circ$ on a glass substrate in Table 2.

In Fig. 5(b), we display the corresponding results for the field enhancements at positions A and B. It is obvious that the general tendency is the same as in the case of the nano-bars, namely that the enhancement increases notably with particle size. Remarkably, the local field enhancements attainable for V-structures under plane wave illumination are slightly below those of nano-bars of same lengths and tip radii (c.f. Fig. 3(b)).

For the V-structure, the tip radius can be varied independently of the arm width. We have

#110638 - $15.00 USD Received 27 Apr 2009; revised 12 Jun 2009; accepted 26 Jun 2009; published 7 Aug 2009

Table 2. Resonance wavelengths λ_{res} and quality factors Q for the lowest frequency resonance of V-structures of different lengths on a glass substrate. For all structures, we have fixed parameters $w = h = 20$nm and $\alpha = 30°$.

l [nm]	100	125	150	175	200
λ_{res} [nm]	662	772	884	994	1106
Q	14.6	13.1	12.3	11.7	11.4

exemplarily computed the field enhancement for V-structures with fixed $w = h = 20$nm and $l = 150$nm and tip radii of $r_{tip} = 8$nm and $r_{tip} = 12$nm. As expected, the enhancement increases with decreasing radius and the resulting field enhancements deviate from those with $r_{tip} = w/2 = 10$nm by approximately $\pm$5-8%.

In addition to the field enhancements at points A and B in front of the tip we also extracted the complete field distributions on resonance. In Fig. 6, we display two corresponding intensity maps: Panel (a) depicts the intensity distribution $|E(x,y)|^2$ in the center plane of the structure, i.e., 10nm above the substrate, and panel (b) depicts the intensity distribution in a plane 30nm above the substrate. These computations reveal a total of three hotspots, two at the ends of the arms and one at the end of the tip of the nano-V.

Apart from the enhancements determined with a continuous wave excitation, we have also performed computations with an ultrafast excitation via a narrow-band Gaussian pulse. The temporal envelope of these pulses was $\exp(-t^2/2\sigma)$ and their spectra were centered at the resonance frequencies of the respective structures. The temporal widths σ were chosen to be three optical cycles. However, according to the discussion of section 4, this does not suffice for the enhancement to saturate. As a result, the recorded peak enhancements have been about a factor of 2/3 smaller than those obtained with the monochromatic excitation.

5.2. ATIR- vs. NIT-spectroscopy

From the experimental side, there exist two spectroscopic approaches for analyzing individual nanostructures that are positioned on a substrate. The more traditional approach is commonly referred to as attenuated total internal reflection (ATIR) spectroscopy and exploits the fact that the presence of a nano-particle at the substrate-air interface leads to scattering of radiation

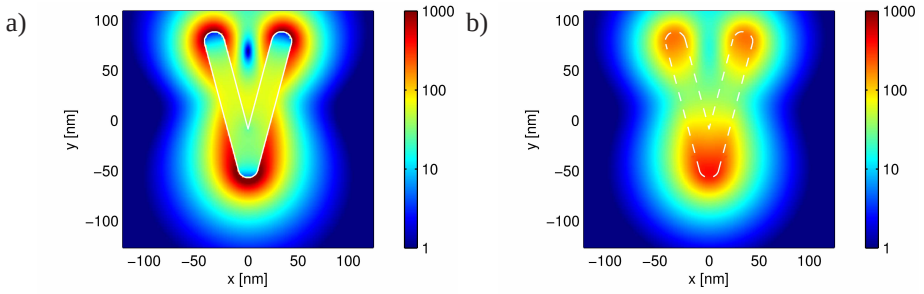

Fig. 6. Intensity distributions $|E(x,y)|^2$ normalized to unit illumination for a monochromatic on-resonance excitation of a silver V with equal width and height $w = h = 20$nm and arm length $l = 150$nm. Panels (a) and (b), respectively, depict the intensity 10nm and 30nm above the substrate. Note that the intensity is displayed on a logarithmic scale.

#110638 - $15.00 USD Received 27 Apr 2009; revised 12 Jun 2009; accepted 26 Jun 2009; published 7 Aug 2009

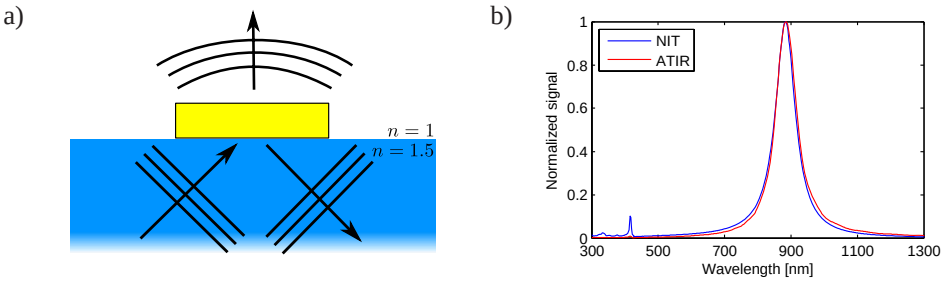

Fig. 7. (a) Sketch of the ATIR geometry. (b) Normalized spectra for NIT- and ATIR-spectroscopy. See text for details.

into the air half-space which, in the absence of the particle, would undergo complete total internal reflection. The scattered radiation can be detected and analyzed. However, the apparent simplicity of the ATIR-setup has the drawback that only relative changes in scattering can be detected and absolute values of cross sections remain elusive [34]. More recently, Arbouet et al. [35] have pioneered a sophisticated modulation technique that allows to detect minute changes in the transmission of a normally incident Gaussian beam that occur when a nano-particle is placed at the beam's focus. In contrast to ATIR-spectroscopy, this normal incidence transmission (NIT) spectroscopy yields absolute values for the extinction cross sections [35,36].

Nevertheless, one might argue that ATIR-spectroscopy provides more detailed information on the scatterer since the corresponding excitation profile provides non-zero wave-vector components parallel to the surface. However, in contrast to grating resonances, particle-plasmon resonances are not directly related to specific wave-vectors so that in the present case of single nano-particle spectroscopy the spectral characteristics of ATIR- and NIT-spectroscopy are nearly identical—except that NIT-spectroscopy provides absolute values. In Fig. 7 we provide the results of our ATIR- and NIT-type computations, normalized to their respective peak values, for the silver nano-V described in Fig. 6. It can be seen that the spectral shape of the main resonance agrees very well, as expected. The discrepancy between the two curves in the region of the higher resonance is rooted in the fact that the ATIR-spectrum is a measure for scattering, while the NIT-spectrum represents extinction, that is the sum of scattering and absorption. At the second resonance, absorption is simply more prominent than at the fundamental one.

5.3. Scaling analysis

Similar to the analysis of nano-bars in section 4.2, we have carried out another scaling analysis for the nano-V geometry. However, the importance of rounded edges for the optical response of nano-Vs (see section 5.1) prevents us from simplifying the geometry in an analogous fashion. As a consequence, we were not able to reach structures in the quasi-static limit within reasonable CPU times. Nevertheless, in Fig. 8 we display the results of scaling a reference structure with $l = 150$nm, $w = h = 25$nm, and $\alpha = 30^\circ$ by a common factor s down to $s = 0.3$. Again, the glass substrate was omitted in these studies. It is obvious that the structures are not yet in the quasi-static limit, since the resonance frequencies exhibit considerable shifts and the absolute values of the scattering cross section for intermediate scaling factors even increase when the structure is scaled down. As a scaling factor of $s = 0.3$ is equivalent to an arm width $w = 7.5$nm, the quasi-static limit seems to be well beyond the reach of current state-of-the-art fabrication techniques.

#110638 - $15.00 USD Received 27 Apr 2009; revised 12 Jun 2009; accepted 26 Jun 2009; published 7 Aug 2009

5.4. *Coherent control via chirped pulses*

Thus far, we have used simple Gaussian wave packets and monochromatic beams in order to excite plasmons in the metallic nanostructures. In principle, excitation schemes based on more complex pulses potentially allow *coherent control* of the optical near-fields, i.e., the interference of plasmon modes within the nanostructure may be tailored in a specific way to achieve a desired response [9]. In this section, we investigate the response of silver nano-Vs to chirped pulses, i.e., Gaussian pulses with varying momentary frequencies as proposed in Refs. [12, 13]. In these works, a calculation within the quasi-static approximation has demonstrated that the spatio-temporal localization properties of the electromagnetic fields may be controlled such that the peak enhancement exceeds that of associated unchirped pulses. In the following, we apply our DGTD framework to treat the problem with a rigorous Maxwell solver that covers the full system dynamics. It should be noted that the spectral complexity of such pulses renders a treatment with conventional frequency-domain finite elements computationally very expensive. Due to its time-domain nature this is not a problem for the framework described here, thereby making it perfectly suitable for the simulation of geometrically complex ultra-fast phenomena.

As an exciting pulse, we take a plane wave with the electric field polarized along the symmetry axis of the nano-V which normally impinges onto the structure from the vacuum halfspace. The corresponding temporal profile is

$$f(t) = \sin\left(\left(1+\beta\frac{\tau}{t_0}\right)\omega_0\tau\right)\exp\left\{-\frac{\tau^2}{2\sigma^2}\right\} \qquad \tau = t - t_0\,. \tag{1}$$

Here, σ denotes the width of the Gaussian envelope and t_0 the time of its maximum amplitude. ω_0 is the central pulse frequency and β represents the chirp parameter. The latter controls the extent to which the momentary frequency varies in time. For $\beta = 0$ we obviously recover a conventional Gaussian pulse. The above expression is valid for $t \in [0, 2t_0]$ and the incident field is taken to be zero otherwise. This of course requires a sufficiently small width σ, such that $f(t = 0, 2t_0) \approx 0$.

The chirped pulses are sent onto silver nano-Vs with length $l = 150$nm, identical width and height $w = h = 20$nm, and apex angle $\alpha = 30^\circ$ located on a glass substrate. Bearing in mind that the idea of coherent control is based on interference, the pulse width σ should be of the order of the life time Q/ω_{res} of the relevant particle plasmon resonance. We set the central frequency of the excitation to the fundamental resonance f_{res} of the V-structure and choose the following

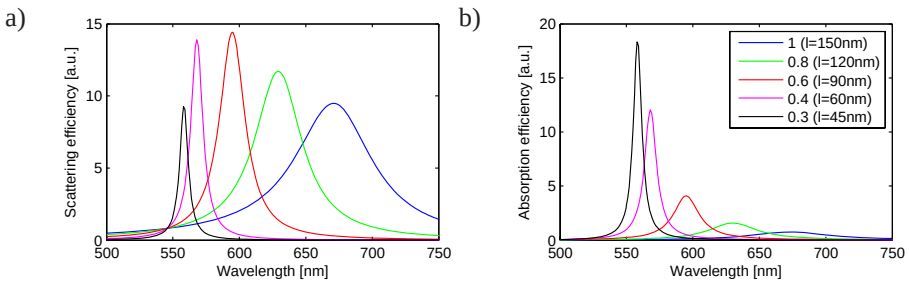

Fig. 8. Scaling analysis for V-structures. The graphs show the behavior of the scattering (panel (a)) and absorption (panel (b)) efficiencies upon scaling a reference V-structure with $l = 150$nm, $w = h = 25$nm, and $\alpha = 30^\circ$ embedded in vacuum with a common factor s given in the legend.

#110638 - $15.00 USD Received 27 Apr 2009; revised 12 Jun 2009; accepted 26 Jun 2009; published 7 Aug 2009

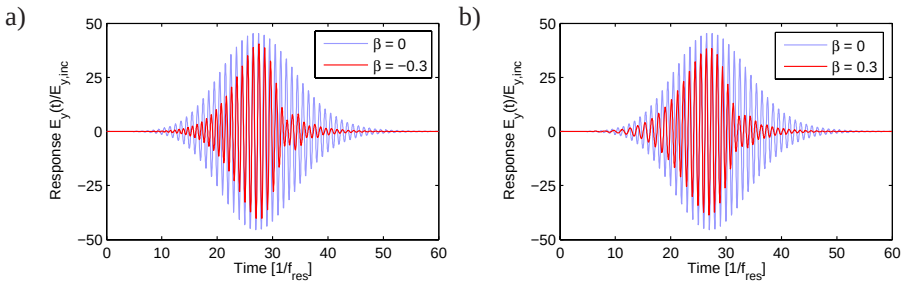

Fig. 9. Response of the structure on chirped pulse excitation for chirp parameters $\beta = -0.3$ (panel (a)) and $\beta = 0.3$ (panel (b)) at point A (1nm from the V's tip and 10nm above the substrate). The parameters of the silver nano-V are $l = 150$nm, $w = h = 20$nm, and $\alpha = 30^\circ$. For reference, we also depict the response to an unchirped pulse ($\beta = 0$). The time is given in units of $1/f_{\rm res} = 2.94$fs, where $f_{\rm res}$ is the resonance frequency of the structure and, at the same time, the central frequency of the pulse.

set of parameters:

$$\omega_0 = 2\pi f_{\rm res}\,, \quad \sigma = 6/f_{\rm res}\,, \quad t_0 = 4\sigma\,. \tag{2}$$

In addition, it is intuitively clear that the presence of the chirp broadens the spectrum of the exciting pulse as compared to a conventional Gaussian pulse. Thus, we have to carefully choose the chirp parameter such that no excitation energy is "wasted" in spectral regions where there is no response from the structure. It shows that for chirp values $|\beta| \lesssim 0.4$, the width of the excitation spectrum does not exceed the width of the particle's spectral response.

In Fig. 9 we display the responses of the V-structure to chirped Gaussian pulses with $\beta = \pm 0.3$. For reference, we also show the response to an unchirped pulse. As a first observation, we note that the magnitude of the response to chirped pulses is less than that of the response to the unchirped excitation. In addition, the envelope of the response is similar to that of the unchirped case until a sudden breakdown occurs just after the response has reached its maximum. We have performed similar computations for chirp parameters $\beta = -0.5 \ldots 0.5$ in steps of 0.1. In all cases, we observe the same qualitative behavior. However, the maximum attainable amplitude decreases with increasing magnitude of the chirp parameter and the breakdown happens more abruptly. Physically, the explanation for this behavior lies in the fact the excitation runs out of phase with the eigenmode that has already been (partly) established during the first half of the pulse. Consequently, at some point the further build-up of the particle-plasmon oscillation is stopped prematurely (as compared to the unchirped case) and an accelerated deexcitation (as compared to the unchirped case) based on destructive interference sets in.

Although one may in some sense speak of a temporal localization of the enhancement as compared to the unchirped pulse, the degree of control exerted on the structure is still not nearly as high as suggested by quasi-static calculations [12, 13]. The reason for this behavior lies in the fact that—outside the quasi-static limit—retardation effects modify and limit the plasmons' abilities to interfere with each other and to produce strong field enhancements. In principle, there exists the possibility to overcome these limitations by allowing for a completely general pulse and to optimize its temporal and polarization profile so as to obtain a prescribed response. A promising route for obtaining a prescribed response has, for instance, been suggested in Ref. [14]. However, there still exists a natural limitation to all efforts in this direction which is set by the spectral width of the structure's spectral response: The narrower the response, the less frequencies are available for shaping the excitation and engineering the response. Working

#110638 - $15.00 USD Received 27 Apr 2009; revised 12 Jun 2009; accepted 26 Jun 2009; published 7 Aug 2009

along these lines, one could try to broaden the fundamental resonance of the V-structure by optimizing geometrical parameters. Alternatively, it is tempting to use more than just the fundamental resonance of the structure in order to engineer a desired optical response. However, due to the fact that the V-structure is very similar to a simple antenna, its second resonance is located at about half the wavelength of the fundamental resonance so that it will be difficult to exploit higher-order resonances via chirped pulses. In turn, this suggests abandoning the idea of using the V-structure altogether and using a more complex geometry instead which provides multiple resonances closely packed in a certain frequency range.

6. Conclusion

In conclusion, we have analyzed silver nano-bars and silver nano-Vs with regard to their optical response and control thereof. For nano-bars, we have identified the onset of the quasi-static limit for bars of lengths $l \lesssim 15$nm. Outside the quasi-static limit, we have found that the attainable values for the field enhancement near nano-bars are about 50% higher than those of nano-Vs of comparable sizes. In this regime, the resonance frequencies and values for the field enhancement strongly depend on the bar or arm length. Furthermore, we have demonstrated that ATIR- and NIT-spectroscopy for these particles essentially provide the same spectral information, except that NIT-spectroscopy is capable of providing absolute values for cross sections. Finally, we have investigated coherent control schemes based on chirped pulse excitations of silver nano-Vs. While we find that a certain degree of control can be exerted, the full electromagnetic analysis suggests that this control is limited and more sophisticated control schemes and/or more complex geometries have to be employed in order to realize strong spatio-temporal localization of radiation in conjunction with large field enhancements.

Acknowledgments
We acknowledge support by the Deutsche Forschungsgemeinschaft (DFG) and the State of Baden-Württemberg through the DFG-Center for Functional Nanostructures (CFN) within subprojects A1.2 and A5.2. The research of M.K. is further supported by a PhD scholarship of the Studienstiftung des Deutschen Volkes. The PhD education of M.K. and J.N. is embedded in the Karlsruhe School of Optics & Photonics (KSOP). K.S. further acknowledges support by the Austrian Science Fund through SFB FOQUS and by the Institute for Quantum Optics and Quantum Information (IQOQI) of the Austrian Academy of Sciences. The DGTD computations have been performed on HP XC4000 at Steinbuch Center for Computing (SCC) Karlsruhe under project NOTAMAX.

#110638 - $15.00 USD Received 27 Apr 2009; revised 12 Jun 2009; accepted 26 Jun 2009; published 7 Aug 2009